


Role of Interlayer in 3D Vertically Aligned Nanocomposite Frameworks with Tunable Magnetotransport Properties

Xing Sun, Matias Kalaswad, Qiang Li, Robynne L. Paldi, Jijie Huang, Han Wang, Xingyao Gao, Xinghang Zhang, and Haiyan Wang*

To investigate the role of interlayers on the growth, microstructure, and physical properties of 3D nanocomposite frameworks, a set of novel 3D vertically aligned nanocomposite (VAN) frameworks are assembled by a relatively thin interlayer (M) sandwiched by two consecutively grown $\text{La}_{0.7}\text{Sr}_{0.3}\text{MnO}_3$ (LSMO)-ZnO VANs layers. ZnO nanopillars from the two VAN layers and the interlayer (M) create a heterogeneous 3D frame embedded in the LSMO matrix. The interlayer (M) includes yttria-stabilized zirconia (YSZ), CeO_2 , SrTiO_3 , BaTiO_3 , and MgO with in-plane matching distances increasing from ≈ 3.63 to ≈ 4.21 Å, and expected in-plane strains ranging from tensile ($\approx 8.81\%$ on YSZ interlayer) to compressive ($\approx -6.23\%$ on MgO interlayer). The metal-insulator transition temperature increases from ≈ 133 K ($M = \text{YSZ}$) to ≈ 252 K ($M = \text{MgO}$), and the low-field magnetoresistance peak value is tuned from $\approx 36.7\%$ to $\approx 20.8\%$. The 3D heterogeneous frames empower excellent tunable magnetotransport properties and promising potentials for microstructure-enabled applications.

Strain engineering has been recognized as an effective approach for tailoring the microstructure and multifunctionalities of materials, including electrical, magnetic, optical properties and more.^[1–5] Different from the substrate-based strain tuning in single-phase epitaxial films that are constrained by the critical film thickness (approximately up to a few tens of nanometers), self-assembled two-phase epitaxial nanocomposite films with various morphologies have offered much more flexibility in microstructural tuning, strain tailoring, and multifunctionalities.^[6–12] Among all the two-phase nanocomposite designs, vertically aligned nanocomposites (VANs) offer high-density vertically aligned interfaces, strain coupling, and strong anisotropic physical properties and have thus attracted great attention.^[3,13–20]

Dr. X. Sun, Dr. Q. Li, R. L. Paldi, Dr. J. Huang, Dr. H. Wang, Dr. X. Gao, Prof. X. Zhang, Prof. H. Wang
School of Materials Engineering
Purdue University
West Lafayette, IN 47907, USA
E-mail: hwang00@purdue.edu
M. Kalaswad, Prof. H. Wang
School of Electrical and Computer Engineering
Purdue University
West Lafayette, IN 47907, USA

 The ORCID identification number(s) for the author(s) of this article can be found under <https://doi.org/10.1002/admi.201901990>.

DOI: 10.1002/admi.201901990

Very recently, a 3D framework design integrating complex VAN structures has drawn great research interest.^[2,6,21,22] The 3D framework is generated by integrating the multilayer and VAN designs together—numerous vertical nanopillars connect with the lateral interlayers to form a 3D interconnected frame embedded in the matrix. This 3D framework design combines the lateral and vertical strain engineering within the film, exhibits both advantages of the multilayer and VAN designs, and achieves an unprecedented degree of control of the film strain and properties.^[6,22]

The 3D framework thin films were first demonstrated in $\text{La}_{0.7}\text{Sr}_{0.3}\text{MnO}_3$ (LSMO)- CeO_2 systems by inserting one to three layers of CeO_2 (or LSMO) interlayers into the LSMO- CeO_2 VAN counterparts and forming 3D CeO_2 (or LSMO) frame-

works.^[6] Later, the feasibility of this 3D framework concept was demonstrated in LSMO-ZnO system along with a study on the effect of the ZnO interlayer thickness, which was controlled from 0 to ≈ 10 nm and effectively tuned the magnetotransport performance of the 3D framework films.^[22] The overall framework (i.e., the secondary interlayers) embedded in all the reported 3D thin films is homogeneous, such as CeO_2 , LSMO, and ZnO.^[6,21,22] Studies on heterogeneous interlayers are still rare. Moreover, the interlayer and its interplay with the matrix material are crucial for the 3D frameworks, since the 3D frames consist of vertical nanopillars and lateral interlayers. To achieve a precise control on the 3D framework structures, understanding the role of the interlayer within the 3D framework is significant and necessary.

In this work, a set of 3D framework thin films have been processed by inserting different lateral interlayers (M). These interlayers present different in-plane matching distances from LSMO as illustrated in Figure 1a. The interlayer M candidates are yttria-stabilized zirconia (YSZ, 8 mol% Y_2O_3 + 92 mol% ZrO_2), CeO_2 , SrTiO_3 (STO), BaTiO_3 (BTO), and MgO. In the resulting 3D structures, all ZnO nanopillars connect with the lateral interlayer M and create a 3D heterogeneous frame embedded in the LSMO matrix. The role of the lateral interlayer in determining the 3D heterogeneous framework microstructure and magnetotransport properties is systematically studied. The aforementioned interlayer materials are selected for the following reasons: 1) the in-plane lattice matching

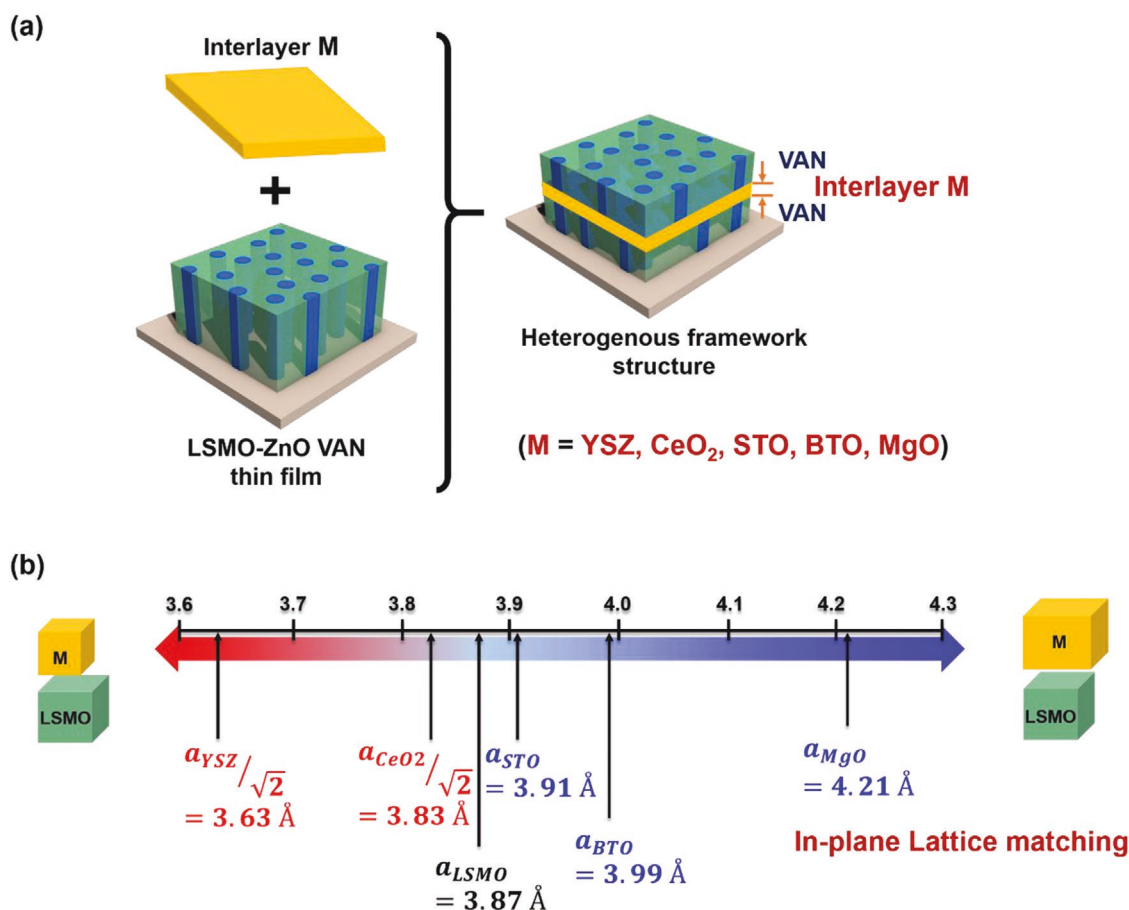


Figure 1. a) Schematic illustration of constructing a 3D heterogeneous framework by inserting a lateral interlayer M (M = YSZ, CeO₂, STO, BTO, or MgO) into a LSMO-ZnO VAN thin film. b) Schematic drawing showing the in-plane matching distance relations within these oxides, for example, YSZ, CeO₂, LSMO, STO, BTO, and MgO.

distance of these oxides gradually increases from 3.63 Å (YSZ), 3.83 Å (CeO₂), 3.91 Å (STO), 3.99 Å (BTO) to 4.21 Å (MgO), which enables the systematical in-plane strain tuning of LSMO ($a_{LSMO} = 3.87 \text{ Å}$) from compressive to tensile strain as illustrated in Figure 1b. 2) These oxides are insulating and can, thus, serve as tunneling barriers to enhance the magnetotransport properties of LSMO. 3) They all have good chemical, mechanical, and thermal stabilities. The chosen oxides also exhibit structural compatibility and have been utilized as the secondary phase in assembling the LSMO-based nanocomposite films with good epitaxial quality.^[3,7,15,16,23–27] The LSMO-ZnO VAN system has been well-investigated and exhibits excellent controllable functionalities, especially its magnetotransport properties.^[28–31] The 3D heterogeneous frame enhances the tunability in the heterogeneous designs of complex VAN structures for controllable functionalities and highlights the significance of strain in in-plane nucleation and growth of the VAN systems. In addition, according to the previous study on the ZnO interlayer thickness effect in the LSMO-ZnO VAN system, a proper interlayer should be a continuous thin layer as an insulating barrier instead of a discontinued film with isolated islands and also sufficiently thin to allow the current to tunnel through. The study found that the $\approx 10 \text{ nm}$ ZnO interlayer isolated the VAN layer, blocked the current, and degraded the magnetotransport

properties of the films.^[22] Therefore, in order to exclude the thickness effect, in this study, the interlayers of diverse materials are controlled at the similar thickness ($\approx 5 \text{ nm}$) by the same number of laser pulses.

To understand the role of the interlayer M on the overall microstructural characteristics, the 3D heterogeneous framework thin films with different interlayers were systematically studied by transmission electron microscopy (TEM), scanning TEM (STEM), and energy-dispersive X-ray spectroscopy (EDS) mapping. **Figure 2a** shows the cross-sectional images of the 3D framework with a continuous $\approx 5 \text{ nm}$ thick STO interlayer. The sequential deposition leads to the vertical stacking of a bottom LSMO-ZnO VAN layer, STO interlayer, and a top LSMO-ZnO VAN layer. All of the vertical ZnO nanopillars from the bottom and top VAN layers attach to the STO interlayer, creating a 3D interconnected heterogeneous frame embedded in the LSMO matrix. This agrees well with the expected design in Figure 1a. The distinct diffraction dots in the corresponding selected area electron diffraction (SAED) pattern (Figure 2b) suggest good epitaxial quality of this 3D VAN framework thin film on STO (001) substrate. The high-resolution STEM (HRSTEM) image in Figure 2c confirms the excellent epitaxial growth of the STO interlayer on the LSMO domain. No misfit dislocations are observed and the LSMO domain in the top VAN layer continues the coherent growth. This 3D

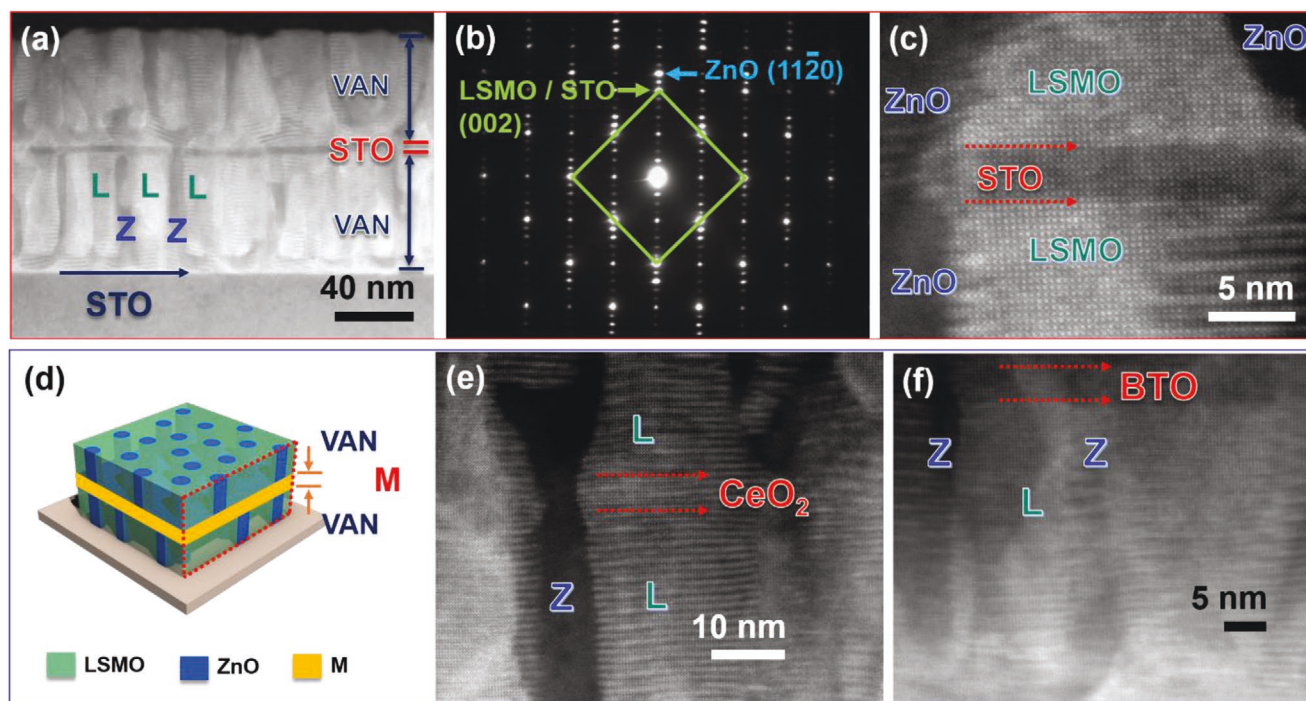


Figure 2. Cross-sectional a) STEM, b) corresponding SAED pattern, and c) HRSTEM images of the 3D heterogeneous framework with a STO interlayer. d) Schematic drawing of the 3D framework with various interlayer M. Cross-sectional HRSTEM images of the 3D frameworks with e) CeO₂ and f) BTO interlayers, respectively.

framework film with an STO interlayer is considered as a reference sample, and the other framework films are fabricated by a similar vertical stacking procedure with the interlayer (M) substituted by other interlayer candidates (Figure 2d), such as BTO and CeO₂. Their corresponding HRSTEM images in Figure 2e,f confirm the epitaxial growth between the interlayer and the VAN layers without misfit dislocations, respectively.

Comparing the aforementioned 3D framework films, each 3D framework microstructure is unique due to the integration of different interlayers (Figure 3). Among all the interlayer candidates, STO ($a_{\text{STO}} = 3.91 \text{ \AA}$) has a better in-plane lattice matching with LSMO ($a_{\text{LSMO}} = 3.87 \text{ \AA}$) (Figure 3a1). Since the STO interlayer is thin and coherently grown, the in-plane strain ($\epsilon_{\text{STO}}^{\text{LSMO}}$) of STO induced from LSMO is calculated to be quite small ($\approx -1.02\%$) according to the following equation

$$\epsilon_{\text{STO}}^{\text{LSMO}} (\%) = \frac{a_{\text{LSMO}} - a_{\text{STO}}}{a_{\text{STO}}} \times 100\% \quad (1)$$

where a_{STO} and a_{LSMO} correspond to the in-plane bulk lattice parameters of STO and LSMO, respectively. $\epsilon_{\text{STO}}^{\text{LSMO}}$ represents the in-plane strain of STO induced from LSMO lattice. In parallel, the in-plane strain of STO induced from ZnO is calculated to be $\approx 1.82\%$. Overall, the strain of STO interlayer derived from coupling with the L3Z7 (molar ratio of LSMO/ZnO = 3:7) VAN layer is calculated to be $\approx 0.96\%$, according to the following equation

$$\epsilon_{\text{STO}}^{\text{L3Z7}} = \epsilon_{\text{STO}}^{\text{LSMO}} \times 0.3 + \epsilon_{\text{STO}}^{\text{ZnO}} \times 0.7 \quad (2)$$

where $\epsilon_{\text{STO}}^{\text{LSMO}}$, $\epsilon_{\text{STO}}^{\text{ZnO}}$, and $\epsilon_{\text{STO}}^{\text{L3Z7}}$ correspond to the strain of STO induced from LSMO, ZnO lattices, and L3Z7 VAN layer,

respectively. The deformation of the STO interlayer is negligible. Therefore, based on the STO interlayer, all the ZnO nanopillars in the top VAN layer are vertically aligned (Figure 3a2,a3), similar as the ones in the bottom VAN layer.

It is noted that the integration of the BTO or CeO₂ interlayer enables the ZnO nanopillars to be inclined from the vertical axis in the top VAN layer (Figure 3b2,c2), even though BTO and CeO₂ interlayers are actually under the opposite strain states in the 3D framework films. In the case of the BTO interlayer, the BTO ($a_{\text{BTO}} = 3.99 \text{ \AA}$) lattice would be under a biaxial compressive strain of $\approx -3.01\%$ after the cube-on-cube growth on LSMO ($a_{\text{LSMO}} = 3.87 \text{ \AA}$) (Figure 3b1). After coupling with the L3Z7 VAN layer, the average strain of BTO interlayer is estimated to be $\approx -1.06\%$ (compressive). Since the BTO interlayer is quite thin ($\approx 5 \text{ nm}$) and epitaxial, the accumulated volume strain energy is not sufficient to nucleate misfit dislocations.^[32] However, the large local strain could lead to surface roughening, generate low-angle misoriented or tilted grains, and increase the structural disorder. This process is caused by the balance between the interfacial energy and elastic strain energy, which has been previously reported.^[9,12] The subsequent VAN layer continues the angled lattice orientation and exhibits tilted ZnO and LSMO nanodomains (Figure 3b2,b3) to minimize the overall strain energy.

Different from all the above cases, the CeO₂ interlayer is calculated under a biaxial tensile strain of $\approx 3.16\%$ in the 3D framework film due to coupling with the VAN layer (Figure 3c1). The ZnO nanopillars are tilted more evidently with a larger tilting angle in the top VAN layer (marked by yellow arrows in Figure 3c2) and the CeO₂ interlayer exhibits a very high surface roughness (Figure 3c3). In addition to the large strain

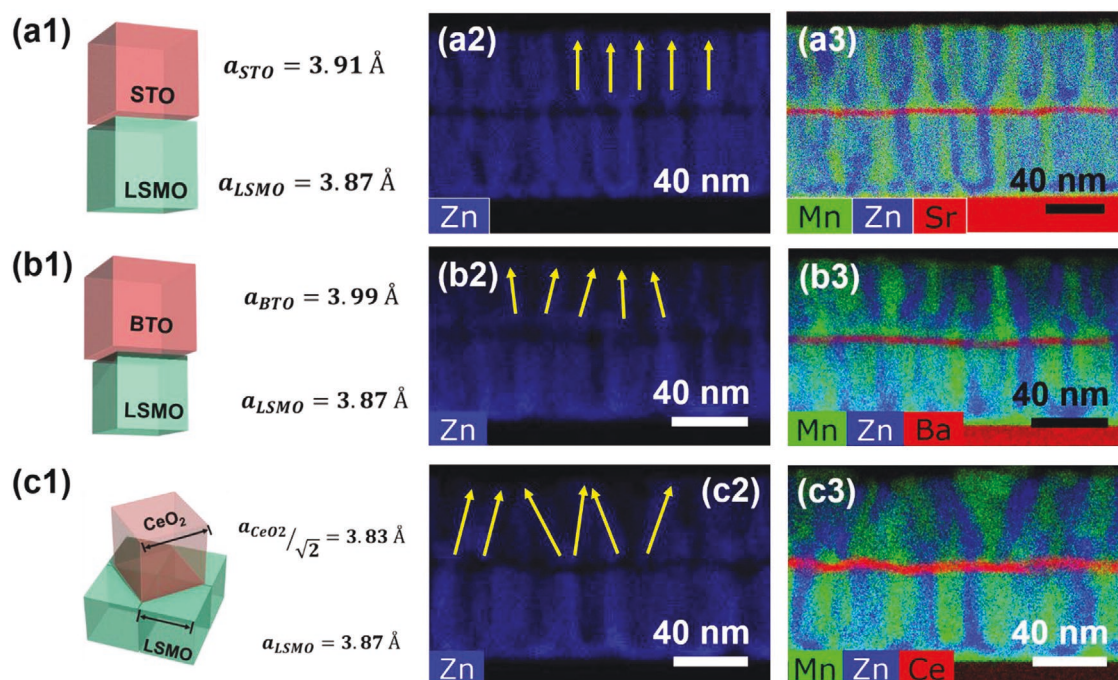


Figure 3. a1) Schematic illustration showing the lattice coupling relation between STO and LSMO. a2,a3) Cross-sectional EDS mapping images of the 3D heterogeneous framework with a STO interlayer. b1) Schematic illustration showing the lattice coupling relation between BTO and LSMO. b2,b3) Cross-sectional EDS mapping images of the 3D framework with a BTO interlayer. c1) Schematic illustration showing the lattice coupling relation between CeO₂ and LSMO. c2,c3) Cross-sectional EDS mapping images of the 3D heterogeneous framework with a CeO₂ interlayer.

accommodation, the 45° in-plane rotation between CeO₂ and LSMO unit cells (Figure 3c1) also facilitates the highly increased surface roughness and buckling of the CeO₂ interlayer (Figure 3c3). Similar phenomena of the tilted growth were observed in a previously reported YSZ-Ce_{0.9}Gd_{0.1}O_{1.95} VAN system.^[33] Meanwhile, the tilted growth of nanodomains is also confirmed in the samples with YSZ (Figure S2, Supporting Information) and MgO (Figure S3, Supporting Information) as the interlayer. Therefore, at low interlayer thickness, the interfacial mismatch can induce the lattice distortion, interlayer roughening, and even tilted growth of nanodomains, regardless whether the interlayer is under tensile or compressive strain.

The influence of the different interlayers on the magnetotransport properties of the 3D heterogeneous frameworks has been investigated and the results are plotted in Figure 4. The resistance of these frameworks in general decreases within the entire temperature regime by switching the interlayer (M) from YSZ to MgO (Figure 4a). As the temperature is increased from 50 to 390 K, the resistance of each framework is enhanced at first and then decreased with a well-defined metal-insulator transition. The corresponding transition temperature (T_{MI}) increases from ≈133 to ≈252 K by varying the interlayer (M) from YSZ to MgO (Figure 4b), highlighting the potential of the tunable magnetoelectric transport properties in 3D heterogeneous frameworks. The variations of the resistance and T_{MI} are mainly attributed to the integration of the interlayer M that serves as the insulating barrier, blocks the electrical transport channels, and restricts the current flow.^[34,35] The enhanced resistance leads to a decreased T_{MI} , which agrees well with the previous reports.^[24,35–39] The temperature dependence of

magnetoresistance (MR%-T) curves of Figure 4c is generated according to the R-T curves in Figure 4a. The maximum MR% (MR_{peak}) value and its position (T_{peak}) of each framework could be tuned by varying the interlayer M. The MR_{peak} value of each 3D framework is gradually reduced from ≈36.7% to ≈20.8% by varying from YSZ to MgO and the YSZ interlayer sample presents the optimized MR properties (Figure 4d). Although the X-ray diffraction (XRD) results do not reveal obvious LSMO peak shifts (Figure S1, Supporting Information), it is believed that the interlayers of different lattice parameters and crystal structures could cause different biaxial interface strain effects on the LSMO domains locally, increase the structural and magnetic spin disorder degrees, and reinforce the grain boundary effects.^[35] Accordingly, the charge carrier scattering and resistance increase under zero magnetic field. Once an external magnetic field of 1 T is applied, the magnetic spins are aligned and the magnetic coupling is strengthened, resulting in reduced resistance and thus improved MR.^[23,31,40,41] The electrons can tunnel through the thin insulating barriers (e.g., ZnO domains and the interlayer M) laterally and vertically, which further boosts the magnetotransport properties.^[6,31] This magnetotunneling effect is closely associated with the electrical properties of the barriers and the barrier-LSMO interfaces. The reduced resistance with the interlayer varied from YSZ to MgO could contribute to the successive decline of the MR_{peak} values.^[42–44] Overall, the 3D heterogeneous frames empower these nanocomposite films with the highly enhanced and controllable MR_{peak} values, compared to the previously reported LSMO epitaxial thin films (≈1–16%) and LSMO-ZnO VAN film (≈20%) (marked in gray rectangle and blue dashed line

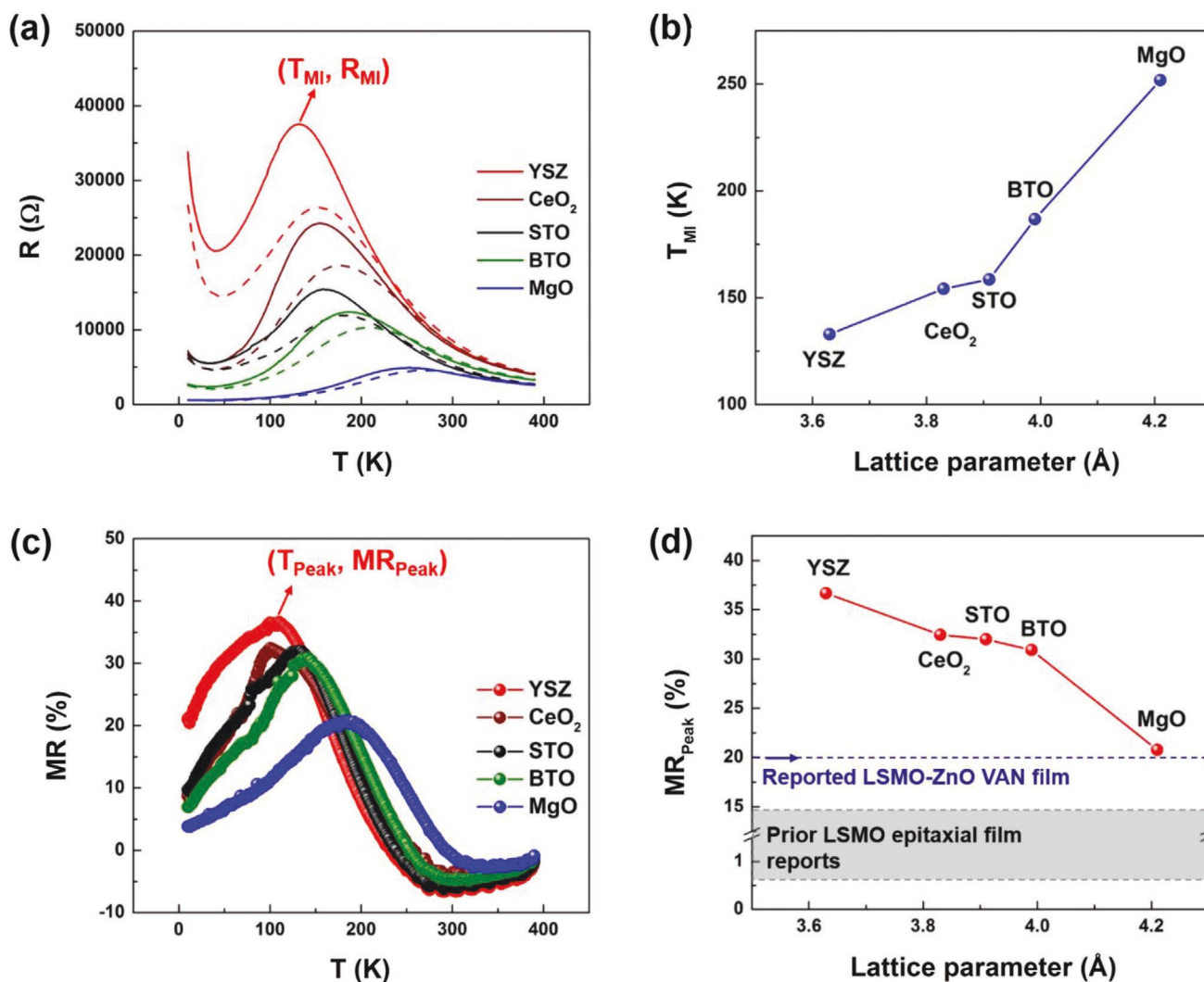


Figure 4. a) Temperature dependence of resistance (R-T) curves for the 3D heterogeneous frameworks with varying the interlayer M (M = YSZ, CeO₂, STO, BTO, MgO) under zero magnetic field (solid line) and an external magnetic field of 1 T (dashed line). b) The evolving curves of the metal-insulator transition temperature (T_{MI}) of these 3D heterogeneous frameworks. c) Temperature dependence of magnetoresistance (MR-T) curves for these 3D heterogeneous frameworks. d) The MR_{peak} value evolution of these 3D heterogeneous framework with the interlayer M varying from YSZ to MgO (the gray rectangular region marks the MR_{peak} range of the previously reported LSMO single-phase epitaxial films that is around 1–16%; the blue dashed line marks the MR_{peak} value of the reported L3Z7 VAN film).^[22,27,41–43]

in Figure 4d).^[22,31,45–47] This new interlayer design provides an effective approach to engineer the microstructure, the overall two-phase morphology, strain, and related physical properties, especially the electrical transport properties.

In summary, a new microstructure embedding a 3D interconnected heterogeneous frame has been achieved in two-phase epitaxial VAN films with different interlayers. More specifically, the 3D interconnected heterogeneous frame is generated by sandwiching a thin interlayer M with two VAN layers of LSMO-ZnO. To explore the significance of the interlayer M on the microstructure and transport properties, the interlayer M material was varied from YSZ, CeO₂, STO, BTO to MgO, with their lateral matching distance increased from 3.63 Å (YSZ) to 4.21 Å (MgO). The interlayer with a high lateral lattice-mismatch causes tilted ZnO nanopillars in the top VAN layer. The interlayer tunes the electrical resistance of the films

and enhances T_{MI} from ≈ 133 to ≈ 252 K. The magnetotransport properties are also highly improved with the MR peak value ramped from $\approx 20.8\%$ (MgO) up to 36.7% (YSZ). The multilayer VAN structures with interlayer designs provide a new approach for complex VAN designs for new or enhanced multifunctionalities with more flexibility in 3D designs and strain tuning.

Experimental Section

The 3D heterogeneous framework samples were deposited on STO (001) substrates using pulsed laser deposition along with a composite LSMO-ZnO target (molar ratio of LSMO/ZnO = 3:7, name as L3Z7) and pure targets of interlayer materials (M = YSZ, CeO₂, STO, BTO, and MgO). The 3D heterogeneous framework samples were prepared through a three-step sequential deposition: 1) depositing one LSMO-ZnO VAN layer onto the STO substrate; 2) depositing

one single-phase M interlayer on the top; and 3) depositing a second LSMO-ZnO VAN layer on top of the M interlayer. During the growth, the substrates were maintained at 750 °C while the targets were ablated with a laser frequency of 10 Hz. The working pressure of deposition was controlled at 200 mTorr of oxygen. When the deposition was finished, the substrates were cooled down to room temperature at 10 °C min⁻¹ under with the oxygen pressure controlled at 200 Torr. Moreover, all the interlayers were grown by the same number of laser pulses (i.e., 60 pulses) during deposition to ensure that the interlayer is formed as a continuous thin barrier with similar thickness (≈5 nm) for each film. Minor interlayer thickness variation could be due to the different growth rates among different oxides.

XRD (PANalytical Empyrean system) was used to analyze the phases and structures of the as-prepared films. The microstructures of these films were studied through TEM (Talos F200X FEG, FEI) at 200 kV equipped with ultrahigh-resolution high-angle annular dark-field and Super-X EDS detectors. A Physical Property Measurement System (Quantum Design) was used to investigate the magnetotransport properties of the films in a four-point probe configuration. The temperature dependence of resistance (R-T) curves was collected with the temperature enhanced from 10 to 390 K under zero magnetic field and an applied magnetic field of 1 T perpendicular to the films surface. The MR value was calculated according to the equation below

$$MR(\%) = \frac{R_0 - R_H}{R_0} \times 100\% \quad (3)$$

where R_0 and R_H represent the resistances collected under zero magnetic field and the magnetic field of 1 T perpendicular to the film surface, respectively.^[2,6,22,38]

Supporting Information

Supporting Information is available from the Wiley Online Library or from the author.

Acknowledgements

This work was funded by the U.S. National Science Foundation (DMR-1565822 for thin film growth and TEM, and ECCS-1902644 for electrical transport measurement).

Conflict of Interest

The authors declare no conflict of interest.

Keywords

3D heterogeneous frame, low-field magnetoresistance, strain-driven tilt, strain relaxation, vertically aligned nanocomposites

Received: November 26, 2019

Revised: February 28, 2020

Published online:

- [1] J. L. MacManus-Driscoll, P. Zerrer, H. Y. Wang, H. Yang, J. Yoon, A. Fouchet, R. Yu, M. G. Blamire, Q. X. Jia, *Nat. Mater.* **2008**, 7, 314.
- [2] X. Sun, Q. Li, J. Huang, M. Fan, B. X. Rutherford, R. L. Paldi, J. Jian, X. Zhang, H. Wang, *Appl. Mater. Today* **2019**, 16, 204.
- [3] A. P. Chen, Z. X. Bi, Q. X. Jia, J. L. MacManus-Driscoll, H. Y. Wang, *Acta Mater.* **2013**, 61, 2783.

- [4] D. G. Schlom, L. Q. Chen, C. J. Fennie, V. Gopalan, D. A. Muller, X. Q. Pan, R. Ramesh, R. Uecker, *MRS Bull.* **2014**, 39, 118.
- [5] R. Roldan, A. Castellanos-Gomez, E. Cappelluti, F. Guinea, *J. Phys.: Condens. Matter* **2015**, 27, 313201.
- [6] X. Sun, J. J. Huang, J. Jian, M. Fan, H. Wang, Q. Li, J. L. MacManus-Driscoll, P. Lu, X. H. Zhang, H. Y. Wang, *Mater. Horiz.* **2018**, 5, 536.
- [7] A. P. Chen, J. M. Hu, P. Lu, T. N. Yang, W. R. Zhang, L. G. Li, T. Ahmed, E. Enriquez, M. Weigand, Q. Su, H. Y. Wang, J. X. Zhu, J. L. MacManus-Driscoll, L. Q. Chen, D. Yarotski, Q. X. Jia, *Sci. Adv.* **2016**, 2, e1600245.
- [8] Y. Zhu, A. Chen, H. Zhou, W. Zhang, J. Narayan, J. L. MacManus-Driscoll, Q. Jia, H. Wang, *APL Mater.* **2013**, 1, 050702.
- [9] X. Weng, M. Hennes, A. Coati, A. Vlad, Y. Garreau, M. Sauvage-Simkin, E. Fonda, G. Patriarche, D. Demaille, F. Vidal, Y. Zheng, *Phys. Rev. Mater.* **2018**, 2, 106003.
- [10] N. Dix, R. Muralidharan, J. M. Rebled, S. Estrade, F. Peiro, M. Varela, J. Fontcuberta, F. Sanchez, *ACS Nano* **2010**, 4, 4955.
- [11] J. MacManus-Driscoll, A. Suwardi, A. Kursumovic, Z. X. Bi, C. F. Tsai, H. Y. Wang, Q. X. Jia, O. J. Lee, *APL Mater.* **2015**, 3, 062507.
- [12] V. Schuler, F. J. Bonilla, D. Demaille, A. Coati, A. Vlad, Y. Garreau, M. Sauvage-Simkin, A. Novikova, E. Fonda, S. Hidki, V. Etgens, F. Vidal, Y. L. Zheng, *Nano Res.* **2015**, 8, 1964.
- [13] A. Chen, Q. Su, H. Han, E. Enriquez, Q. Jia, *Adv. Mater.* **2019**, 31, 1803241.
- [14] S. Lee, J. L. MacManus-Driscoll, *APL Mater.* **2017**, 5, 042304.
- [15] W. R. Zhang, A. P. Chen, Z. K. Bi, Q. X. Jia, J. L. MacManus-Driscoll, H. Y. Wang, *Curr. Opin. Solid State Mater. Sci.* **2014**, 18, 6.
- [16] J. J. Huang, J. L. MacManus-Driscoll, H. Y. Wang, *J. Mater. Res.* **2017**, 32, 4054.
- [17] X. M. Ma, Z. L. Liao, L. LiP. Gao, *Adv. Mater. Interfaces* **2017**, 4, 1700225.
- [18] M. Acosta, F. Baiutti, A. Tarancon, J. L. MacManus-Driscoll, *Adv. Mater. Interfaces* **2019**, 6, 1900462.
- [19] X. K. Ning, Z. J. Wang, Z. D. Zhang, *Adv. Mater. Interfaces* **2015**, 2, 1500302.
- [20] Y. M. Zhu, T. H. Do, V. T. Tra, R. Yu, Y. H. Chu, Q. Zhan, *Adv. Mater. Interfaces* **2018**, 5, 1701202.
- [21] A. Chen, Z. Harrell, P. Lu, E. Enriquez, L. Li, B. Zhang, P. Dowden, C. Chen, H. Wang, J. L. MacManus-Driscoll, Q. Jia, *Adv. Funct. Mater.* **2019**, 29, 1900442.
- [22] X. Sun, Q. Li, J. Huang, J. Jian, P. Lu, X. Zhang, J. L. MacManus-Driscoll, H. Wang, *J. Appl. Phys.* **2019**, 125, 082530.
- [23] H. Yang, Z. E. Cao, X. Shen, T. Xian, W. J. Feng, J. L. Jiang, Y. C. Feng, Z. Q. Wei, J. F. Dai, *J. Appl. Phys.* **2009**, 106, 104317.
- [24] V. Moshnyaga, B. Damaschke, O. Shapoval, A. Belenchuk, J. Faupel, O. I. Lebedev, J. Verbeeck, G. Van Tendeloo, M. Mucksch, V. Tsurkan, R. Tidecks, K. Samwer, *Nat. Mater.* **2003**, 2, 247.
- [25] O. I. Lebedev, J. Verbeeck, G. Van Tendeloo, O. Shapoval, A. Belenchuk, V. Moshnyaga, B. Damaschke, K. Samwer, *Phys. Rev. B* **2002**, 66, 104421.
- [26] V. Garcia, M. Bibes, L. Bocher, S. Valencia, F. Kronast, A. Crassous, X. Moya, S. Enouz-Vedrenne, A. Gloter, D. Imhoff, C. Deranlot, N. D. Mathur, S. Fusil, K. Bouzehouane, A. Barthelémy, *Science* **2010**, 327, 1106.
- [27] Q. Su, D. Yoon, Z. Sisman, F. Khatkhatay, Q. X. Jia, A. Manthiram, H. Y. Wang, *Int. J. Hydrogen Energy* **2013**, 38, 16320.
- [28] A. P. Chen, M. Weigand, Z. X. Bi, W. R. Zhang, X. J. Lu, P. Dowden, J. L. MacManus-Driscoll, H. Y. Wang, Q. X. Jia, *Sci. Rep.* **2014**, 4, 5426.
- [29] W. R. Zhang, A. P. Chen, F. Khatkhatay, C. F. Tsai, Q. Su, L. Jiao, X. H. Zhang, H. Y. Wang, *ACS Appl. Mater. Interfaces* **2013**, 5, 3995.
- [30] B. S. Kang, H. Wang, J. L. MacManus-Driscoll, Y. Li, Q. X. Jia, I. Mihut, J. B. Betts, *Appl. Phys. Lett.* **2006**, 88.

- [31] A. P. Chen, W. R. Zhang, J. Jian, H. Y. Wang, C. F. Tsai, Q. Su, Q. X. Jia, J. L. MacManus-Driscoll, *J. Mater. Res.* **2013**, 28, 1707.
- [32] K. L. Kavanagh, I. Saveliev, M. Blumin, G. Swadener, H. E. Ruda, *J. Appl. Phys.* **2012**, 111, 044301.
- [33] Q. Su, D. Yoon, A. P. Chen, F. Khatkhatay, A. Manthiram, H. Y. Wang, *J. Power Sources* **2013**, 242, 455.
- [34] A. Gaur, G. D. Varma, *Solid State Commun.* **2006**, 139, 310.
- [35] S. Karmakar, S. Taran, B. K. Chaudhuri, H. Sakata, C. P. Sun, C. L. Huang, H. D. Yang, *J. Phys. D: Appl. Phys.* **2005**, 38, 3757.
- [36] M. Fan, W. R. Zhang, F. Khatkhatay, L. G. Li, H. Y. Wang, *J. Appl. Phys.* **2015**, 118, 065302.
- [37] B. X. Huang, Y. H. Liu, R. Z. Zhang, Xiaobo-Yuan, C.-J. Wang, L.-M. Mei, *J. Phys. D: Appl. Phys.* **2003**, 36, 1923.
- [38] M. Fan, H. Wang, S. Misra, B. Zhang, Z. M. Qi, X. Sun, J. J. Huang, H. Y. Wang, *ACS Appl. Mater. Interfaces* **2018**, 10, 5779.
- [39] L. E. Hueso, J. Rivas, F. Rivadulla, M. A. Lopez-Quintela, *J. Appl. Phys.* **2001**, 89, 1746.
- [40] A. P. Chen, Z. X. Bi, C. F. Tsai, J. Lee, Q. Su, X. H. Zhang, Q. X. Jia, J. L. MacManus-Driscoll, H. Y. Wang, *Adv. Funct. Mater.* **2011**, 21, 2423.
- [41] Z. X. Bi, E. Weal, H. M. Luo, A. P. Chen, J. L. MacManus-Driscoll, Q. X. Jia, H. Y. Wang, *J. Appl. Phys.* **2011**, 109, 054302.
- [42] J. M. De Teresa, A. Barthelemy, A. Fert, J. P. Contour, R. Lyonnet, F. Montaigne, P. Seneor, A. Vaures, *Phys. Rev. Lett.* **1999**, 82, 4288.
- [43] J. M. De Teresa, A. Barthelemy, A. Fert, J. P. Contour, F. Montaigne, P. Seneor, *Science* **1999**, 286, 507.
- [44] S. S. P. Parkin, C. Kaiser, A. Panchula, P. M. Rice, B. Hughes, M. Samant, S. H. Yang, *Nat. Mater.* **2004**, 3, 862.
- [45] A. P. Chen, Z. X. Bi, H. Hazariwala, X. H. Zhang, Q. Su, L. Chen, Q. X. Jia, J. L. MacManus-Driscoll, H. Y. Wang, *Nanotechnology* **2011**, 22, 315712.
- [46] C. H. Yan, Z. G. Xu, T. Zhu, Z. M. Wang, F. X. Cheng, Y. H. Huang, C. S. Liao, *J. Appl. Phys.* **2000**, 87, 5588.
- [47] A. P. Chen, Z. X. Bi, C. F. Tsai, L. Chen, Q. Su, X. H. Zhang, H. Y. Wang, *Cryst. Growth Des.* **2011**, 11, 5405.